Prediction Capability of RANS Turbulence Models for Asymmetrically Heated High-Aspect-Ratio Duct Flows

Kaller, Thomas; Hickel, Stefan; Adams, Nikolaus A.

DOI
10.2514/6.2020-0354

Publication date
2020

Document Version
Final published version

Published in
AIAA Scitech 2020 Forum

Citation (APA)
Kaller, T., Hickel, S., & Adams, N. A. (2020). Prediction Capability of RANS Turbulence Models for Asymmetrically Heated High-Aspect-Ratio Duct Flows. In *AIAA Scitech 2020 Forum: 6-10 January 2020, Orlando, FL* Article AIAA 2020-0354 (AIAA Scitech 2020 Forum; Vol. 1 PartF). American Institute of Aeronautics and Astronautics Inc. (AIAA). https://doi.org/10.2514/6.2020-0354

AIAA SciTech Forum
6-10 January 2020, Orlando, FL
AIAA Scitech 2020 Forum

10.2514/6.2020-0354

Prediction Capability of RANS Turbulence Models for Asymmetrically Heated High-Aspect-Ratio Duct Flows

Thomas Kaller[1], Stefan Hickel[2] and Nikolaus A. Adams[3]
[1,3]*Technical University of Munich, Department of Mechanical Engineering, 85748 Garching, Germany*
[2]*Technische Universiteit Delft, Faculty of Aerospace Engineering, 2629 HS Delft, The Netherlands*

We present well-resolved RANS simulations of a high-aspect-ratio generic cooling duct configuration consisting of an adiabatic straight feed line followed by a heated straight section ending with a 90° bend. The configuration is asymmetrically heated with a temperature difference of $\Delta T = 40\,\mathrm{K}$. As fluid liquid water is used at a Reynolds number of $Re_b = 110 \times 10^3$. The setup follows an experimental reference case, which has also been investigated using a well-resolved LES. The current investigation focuses on the prediction capabilities of different RANS turbulence closure models for the duct flow field, defined by the interaction of secondary flows and turbulent heat transfer. In the straight duct only turbulence-induced secondary flow is present, which becomes weaker along the heated duct due to the viscosity reduction, leading in turn to a reduced mixing. In the curved section, the stronger pressure-induced secondary flow superimposes the turbulence-induced one increasing the mixing of hot and cold fluid. A well-resolved LES serves as comparison database for the straight duct results.

Nomenclature

$[L_x, L_y, L_z]$	Dimensions in x-,y- and z-direction	d_h	Hydraulic diameter
AR	Duct aspect ratio	$[u, v, w]$	Velocity in x-,y- and z-direction
p	Pressure	ρ	Density
T	Temperature	ν	Kinematic viscosity
Re	Reynolds number	Re_τ	Friction Reynolds number
Nu	Nusselt number	Pr	Prandtl number
Pr_t	Turbulent Prandtl number	ν_t	Turbulent eddy viscosity
α_t	Turbulent eddy diffusivity	τ_w	Wall shear stress
u_τ	Friction velocity	q	Heat flux
T_τ	Friction temperature	B_q	Heat flux parameter
Subscript		*Superscript*	
per	periodic section	$(\bar{\cdot})$	Temporally averaged quantity
heat	heated section	$(\cdot')$	Fluctuating quantity
w	wall quantity	$(\cdot^+)$	Viscous wall unit quantity
b	bulk quantity		
c	center quantity		

I. Introduction

Understanding turbulent flow and heat transfer through high aspect ratio cooling ducts (HARCDs) of rectangular cross-section is of great interest for many technical applications. Examples include ventilation systems, electrical component cooling or structural cooling of launcher propulsion systems.

---

[1] Research Associate, Technical University of Munich, Institute of Aerodynamics and Fluid Mechanics, Boltzmannstr. 15, 85748 Garching, Germany

[2] Full Professor, Technische Universiteit Delft, Faculty of Aerospace Engineering, Kluyverweg 1, 2629 HS Delft, The Netherlands

[3] Full Professor, Technical University of Munich, Institute of Aerodynamics and Fluid Mechanics, Boltzmannstr. 15, 85748 Garching, Germany. Member AIAA

The HARCD flow field is characterized by cross-sectional secondary flow structures perpendicular to the main flow direction, which intensify the mixing and enhance heat transfer. Within this study the following two types of secondary flows are considered:

- Prandtl's flow of the first kind, also known as skew-induced or pressure-driven secondary flow, see figure 1 (*b*). This cross-sectional flow is relatively strong. Depending on the curvature radius, respectively the associated radial pressure gradients and centrifugal forces, it can reach values of up to $20-30\%$ of the bulk flow velocity, [1]. The secondary flow field consists of two counter-rotating so-called Dean vortices, each of them spanning one half of the entire cross-section. Prandtl's flow of the first kind may form in laminar and turbulent flows through geometries of rectangular or round cross-section with a cross-sectional pressure gradient being present and it is absent in straight ducts due to the lack thereof.
- Prandtl's flow of the second kind, also known as turbulence-induced secondary flow, see figure 1 (*a*). This cross-sectional flow is relatively weak with a strength of $1-3\%\,u_b$, [2], and forms due to the anisotropy of the Reynolds stress tensor. Hence, it is present in all turbulent flows through geometries of angular cross-section and absent in laminar flows and pipe flows. For a rectangular duct this secondary flow consists of a pair of counter-rotating vortices in each of the corners, transporting fluid from the duct core into the respective corner region.

Another relevant secondary flow type for heated fluids at low Reynolds number is buoyancy-driven secondary flow, which is neglected within the present study due to the high flow velocities. In realistic applications all types of secondary flows interact with each other, exhibiting a significant influence on the momentum and heat transport within cooling ducts. Moreover, secondary flow generation is often promoted by specifically designed vortex generators.

For turbulent flow simulations three main classes are distinguished: the direct numerical simulation (DNS), the large-eddy simulation (LES) and the Reynolds-averaged Navier-Stokes simulation (RANS). In DNS, all spatial and temporal scales of the turbulence spectrum are fully resolved and no turbulence model is required. For the simulation of technical relevant high Re flows a very fine grid resolution is required, rendering a DNS infeasible. In LES, the large turbulent structures containing most of the energy are resolved, whereas the small scales or subgrid-scales (SGS) are modelled. Despite the high numerical cost for high Re flows, LES has become more and more important over the last years. Using the RANS approach, the Navier-Stokes equations (NSE) are solved approximately for the averaged state, whereas LES and DNS produce individual time samples. All scales of the turbulence spectrum are modelled offering the computationally most inexpensive option for the simulation of high Re flows. By averaging the NSE the unknown Reynolds stress tensor $\overline{u_i'u_j'}$ in the momentum equations and the unknown turbulent heat flux vector $\overline{u_i'h'}$ in the energy equation emerge. To close the equation system, i.e. to derive an approximation for the Reynolds stresses, two main turbulence model classes are utilized: Models based on the Boussinesq turbulent viscosity hypothesis and isotropic turbulence closure, so called eddy viscosity models (EVM), and Reynolds stress models (RSM). For the former $\overline{u_i'u_j'}$ is modelled analogous to the molecular stress tensor and $0-2$ additional transport equations are solved to model the turbulent viscosity. The RSMs are computationally more expensive as an additional transport equation for each tensor component is solved. However, they are able to account for turbulence anisotropy relevant for Prandtl's flow of the second kind. For the unknown heat fluxes $\overline{u_i'h'}$ also several approximations exist. The most prevalent is using a simple gradient transport approach with a constant turbulent Prandtl number assumption, linking the turbulent diffusivity to the turbulent viscosity $\alpha_t = \nu_t/Pr_t$. However, several studies have shown this assumption to be invalid for heated duct and other flow configurations, [3–5]. Daly and Harlow [6] and Younis et al. [7] proposed algebraic turbulent heat flux closure models based on the Reynolds stress tensor, which have been applied by Rochhausen [8] for turbomachinery cooling flows. Moreover, for each component of $\overline{u_i'h'}$ an additional transport equations can be solved.

First experimental square duct flow measurements have been performed by Baines and Brundrett [9] and Gessner and Jones [10]. Monty [11] investigated the flow field in high aspect ratio ducts with $AR = 11.7$. First square duct DNS have been performed by Gavrilakis [12] and Huser and Biringen [13], and LES by Madabhushi and Vanka [14]. Vinuesa et al. [15] investigated aspect ratio effects for ducts of $AR = 1-7$. Salinas-Vásquez and Métais [2] analyzed the influence of asymmetrical wall heating in a square duct and Choi and Park [16] the turbulent heat transfer for rectangular ducts of $AR = 0.25$ to $AR = 1.5$. Recently Pirozzoli et al. [17] presented an in-depth analysis of turbulence-induced secondary flow in periodic square ducts. All previous simulations have been performed at relatively low Reynolds number and assuming streamwise periodicity. Relevant RANS studies for cooling duct flows for realistic configurations include Pizzarelli et al. [18, 19, 20].

In the present study a generic asymmetrically heated HARCD at $Re_b = 110\cdot10^3$ and moderate heating ($T_w - T_b = 100\,\mathrm{K} - 60\,\mathrm{K} = 40\,\mathrm{K}$) is investigated numerically using different RANS turbulence closure models available within ANSYS CFX. This setup has been extensively studied experimentally, [21, 22], as well as numerically using a

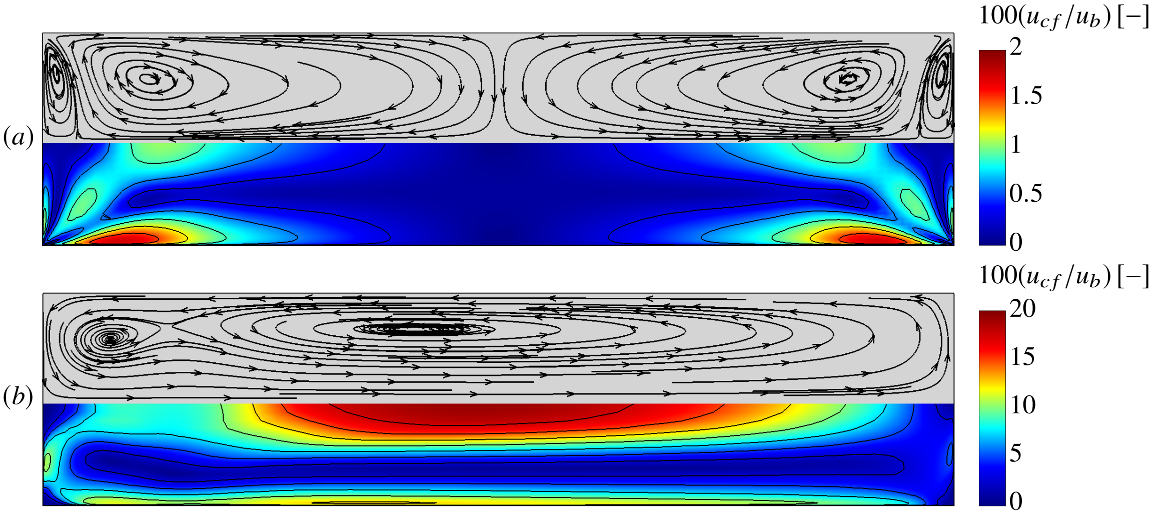

Fig. 1 Crossflow velocity for (a) turbulence-induced ($u_{cf} = \sqrt{v^2 + w^2}$) and ($b$) interaction of turbulence- and pressure-induced secondary flow after a 90° bend ($u_{cf} = \sqrt{u^2 + w^2}$). The inner radius side is on the left.

well-resolved LES, [5, 23, 24]. The latter serves as a database to compare the accuracy of different RANS models including turbulent heat flux closure models. The applied models are the two-equation SST, the explicit algebraic Reynolds stress model BSL EARSM and the full Reynolds stress models SSG RSM and BSL RSM. For the latter several heat flux closure models are investigated, namely the isotropic constant Pr_t assumption, the anisotropic algebraic Daly-Harlow and Younis model, and employing additional transport equations for the turbulent heat fluxes.

II. Equation System and Numerical Model

For the RANS simulations the compressible NSE with the total energy equation are used as implemented in ANSYS CFX, [25]. The fluid properties are evaluated based on the IAPWS IF97 formulation. To close the RANS equation system a turbulence model is required to approximate $\rho\overline{u_i'u_j'}$ in the momentum equations and $\rho\overline{u_i'h'}$ in the total energy equation. Within the current study the following turbulence models are utilized:

- SST: The SST is a two-equation EVM combining a low-Re $k-\omega$-formulation close to walls and a $k-\varepsilon$-formulation in the free stream. Two additional partial differential equations (PDEs) are solved to derive the isotropic turbulent viscosity ν_t.
- BSL RSM: The BSL RSM is an ω-based low-Re Reynolds stress model. For every component of $\rho\overline{u_i'u_j'}$ and the specific dissipation ω an additional PDE is solved. Hence, turbulence anisotropy can be represented.
- SSG RSM: The SSG RSM is an ε-based Reynolds stress model. For every component of $\rho\overline{u_i'u_j'}$ and the dissipation ε an additional PDE is solved. Hence, turbulence anisotropy can be represented.
- BSL EARSM: The BSL EARSM is an extension of classical two-equation models derived from the Reynolds stress transport equations. It features a nonlinear relation between modelled Reynolds stresses and mean strain-rate and vorticity. Hence, it is able to represent secondary flows without having to solve additional PDEs.

All ω-based low-Re models are used with the automatic wall treatment functionality. Further details can be found in Wilcox [26] and ANSYS, Inc. [25, 27].

For modelling $\rho\overline{u_i'h'}$ the following options are applied within the current study:

- Gradient approach with $Pr_t = const.$: standard model within ANSYS CFX. The heat fluxes are related to the mean enthalpy gradients via the isotropic turbulent diffusivity α_t with $\alpha_t = \nu_t/Pr_t$.
- Second moment closure model: An additional PDE is solved for each component of $\rho\overline{u_i'h'}$. Note, that this is a beta feature within ANSYS CFX (CADFEM GmbH, personal communication, 3rd December 2018).
- Algebraic Daly-Harlow model, [6]: An anisotropic turbulent diffusivity tensor is derived proportional to the Reynolds stress tensor:

$$-\overline{u_i'h'} = c_{DH}\,\frac{k}{\varepsilon}\,\overline{u_i'u_j'}\,\frac{\partial\overline{h}}{\partial x_j} \tag{1}$$

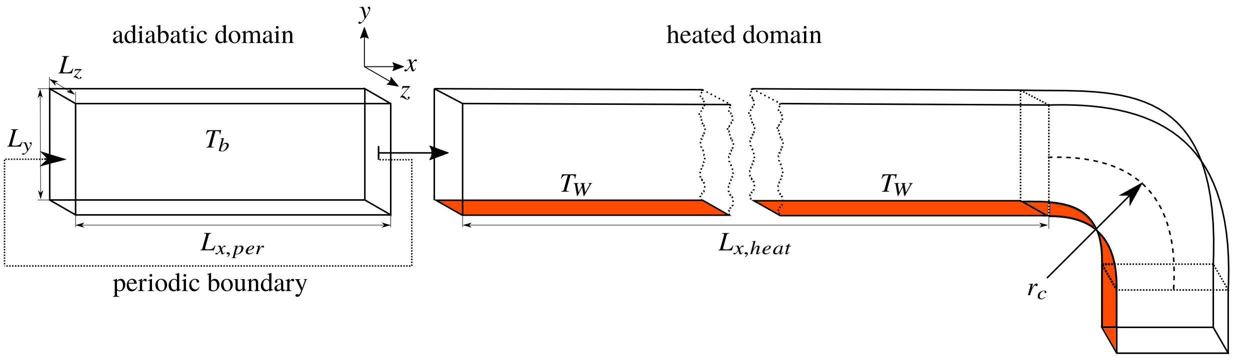

Fig. 2 Setup and geometry for the RANS simulations.

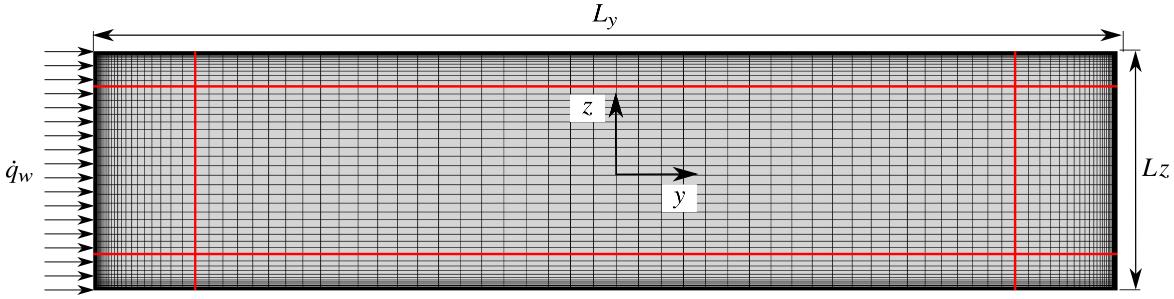

Fig. 3 Cross-sectional mesh and blocking.

with $c_{DH} = 0.3$.

- Algebraic Younis model, [7]: A more accurate anisotropic turbulent diffusivity tensor is derived as

$$-\overline{u_i'h'} = c_{Y1}\frac{k^2}{\varepsilon}\frac{\partial\overline{h}}{\partial x_i} + c_{Y2}\frac{k}{\varepsilon}\overline{u_i'u_j'}\frac{\partial\overline{h}}{\partial x_j} + c_{Y3}\frac{k^3}{\varepsilon^2}\frac{\partial\overline{u}_i}{\partial x_j}\frac{\partial\overline{h}}{\partial x_j} + c_{Y4}\frac{k^2}{\varepsilon^2}\left(\overline{u_i'u_k'}\frac{\partial\overline{u}_j}{\partial x_k} + \overline{u_j'u_k'}\frac{\partial\overline{u}_i}{\partial x_k}\right)\frac{\partial\overline{h}}{\partial x_j} \qquad (2)$$

with $c_{Y1} = -4.55 \cdot 10^{-2}$, $c_{Y2} = 3.73 \cdot 10^{-1}$, $c_{Y3} = -3.73 \cdot 10^{-3}$ and $c_{Y4} = -2.35 \cdot 10^{-2}$.

For the LES database of Kaller et al. [5] the incompressible NSE with the Boussinesq approximation are applied, which is valid for small density variations. The temperature-dependent transport properties are evaluated using the IAPWS correlations. The system is discretized by a fractional step method on a block structured staggered Cartesian grid. For time discretization a third-order Runge-Kutta scheme with $CFL = 1$ is used. A second-order finite-volume method is utilized for spatial discretization. We perform an implicit LES, i.e. the size of the subgrid scales (SGS) is determined by the chosen grid resolution. As SGS model the adaptive local deconvolution method (ALDM) is used, [28, 29]. For further details we refer to Kaller et al. [5].

III. Simulation Setup

The numerical setup is shown in figure 2 and the cross-sectional grid in figure 3. The setup consists of two domains simulated independently. The adiabatic periodic section has a dimension of $50 \times 25.8 \times 6\,\text{mm}^3$, and the heated section consists of a $600 \times 25.8 \times 6\,\text{mm}^3$ straight part followed by a 90° heated bend with a curvature radius of $r_c = 60\,\text{mm}$ and a $50 \times 25.8 \times 6\,\text{mm}^3$ coarsely meshed outlet piece. To determine the required resolution for a wall-resolved RANS simulation, i.e. $y+ \approx 1$, an extensive grid sensitivity study has been performed for the adiabatic periodic section using the BSL EARSM turbulence model. The grid is asymmetric with respect to the z-axis to account for the wall heating and the temperature boundary layer. Hence, the grid is refined at the lower heated wall. In total $34 \times 115 \times 64 = 250240$ nodes are used for the adiabatic periodic and $512 \times 115 \times 64 = 3768320$ nodes for the heated domain. For an accuracy assessment of the well-resolved RANS simulation, we refer to the comparison of an adiabatic square duct RANS at a comparable grid resolution as the cooling duct simulation with LES and DNS results in the appendix.

The adiabatic periodic duct serves to generate a fully developed turbulent HARCD inflow profile for the spatially resolved heated domain. The simulation is performed with liquid water treated as incompressible with fixed fluid

Turbulence model	Turbulence anisotropy	Turbulent heat flux closure	Turbulent Prandtl number
SST EVM	isotropic	Eddy Diffusivity	$Pr_t = 0.9$
BSL EARSM	anisotropic	Eddy Diffusivity	$Pr_t = 0.9$
SSG RSM	anisotropic	Eddy Diffusivity	$Pr_t = 0.9$
		Anisotropic Diffusion	variable Pr_t $C_{ani.\ diff} = 0.244444$ $C_{cross.\ deriv} = 1.0$
BSL RSM	anisotropic	Eddy Diffusivity	$Pr_t = 0.85$
		Eddy Diffusivity	$Pr_t = 0.9$
		Transport Equation	variable Pr_t
		Daly-Harlow model (algebraic)	variable Pr_t
		Younis model (algebraic)	variable Pr_t

Table 1 Turbulence closure model combinations used within the current study. For the turbulence and heat flux closure models the names as specified within ANSYS CFX are used. Exceptions are the algebraic heat flux closure models, which are not available within the program package and added as functional expressions.

properties at $T_b = 333.15\,\mathrm{K}$. All walls are defined as smooth adiabatic walls. In streamwise direction a periodic boundary condition is set with a constant mass flow of $\dot{m} = 0.8193\,\mathrm{kg/s}$ corresponding to $u_b = 5.3833\,\mathrm{m/s}$, respectively $Re_b = 110 \cdot 10^3$. For each turbulence model included within this study, see table 1 for the model combinations, the following procedure is executed: based on an initial solution of $(u/v/w) = (5.3833/0/0)\,\mathrm{m/s}$ a physical time step of $\Delta t = 10^{-5}$ s is used for ≈ 20 iterations. Then a local time scale factor of 50 and reduced pressure update multiplier from the default 0.25 to 0.01 is utilized until a RMS target value of $1 \cdot 10^{-6}$ is surpassed for the momentum and continuity equation residuals.

For the spatially resolved heated duct simulations the compressible NSE as described in section II are used. All walls are treated as smooth walls with the automatic wall treatment option applied. The lower wall is an isothermal wall with $T_W = 373.15\,\mathrm{K}$ and the remaining are adiabatic walls. With the bulk flow temperature of $T_b = 333.15\,\mathrm{K}$ this results in a moderate temperature difference of 40 K. At the inlet, the velocity and turbulence profile extracted from the respective precursor simulation is prescribed. At the outlet a mass flow of $\dot{m} = 0.8193\,\mathrm{kg/s}$ is specified to generate a first solution. Based on this result a second simulation is performed with a prescribed average pressure over the whole outlet of $p_{out} = 101325\,\mathrm{Pa}$ to obtain a physically valid pressure field within the domain. This approach has been chosen to accelerate overall convergence. For each turbulence model included within this study, see table 1 for the model combinations, the following procedure is executed: initially a physical time step of $\Delta t = 10^{-5}$ s is used for 10 iterations. Note, that no specific domain initialization is set. Then a local time scale factor of 25 is utilized for further 15 iterations, after which it is increased to a factor of 50 until a RMS target value of $1 \cdot 10^{-6}$ is surpassed for the momentum, continuity and total energy equation residuals. Based on this result the outlet boundary condition is modified and the simulation restarted with a local time scale factor of 50 until convergence is reached.

IV. Results

In the following sections the results of the RANS simulations for the different turbulence closure model combinations are presented and compared against the LES. First the straight adiabatic periodic HARCD flow field is investigated with a strong focus on the turbulence-induced secondary flow. Then we discuss the results for the asymmetrically heated HARCD focusing on the cross-section $x = 500$ mm close to the end of the straight section, but not yet affected by the downstream bend. In contrast to the adiabatic duct, the heated duct investigation is expanded to include different turbulent heat flux closure models. In the last section the flow and temperature field of the curved section is presented focusing an the duct end cross-section, in which pressure-induced secondary flow dominates the momentum and heat transfer. Note, for the curved section LES results are currently not available for comparison.

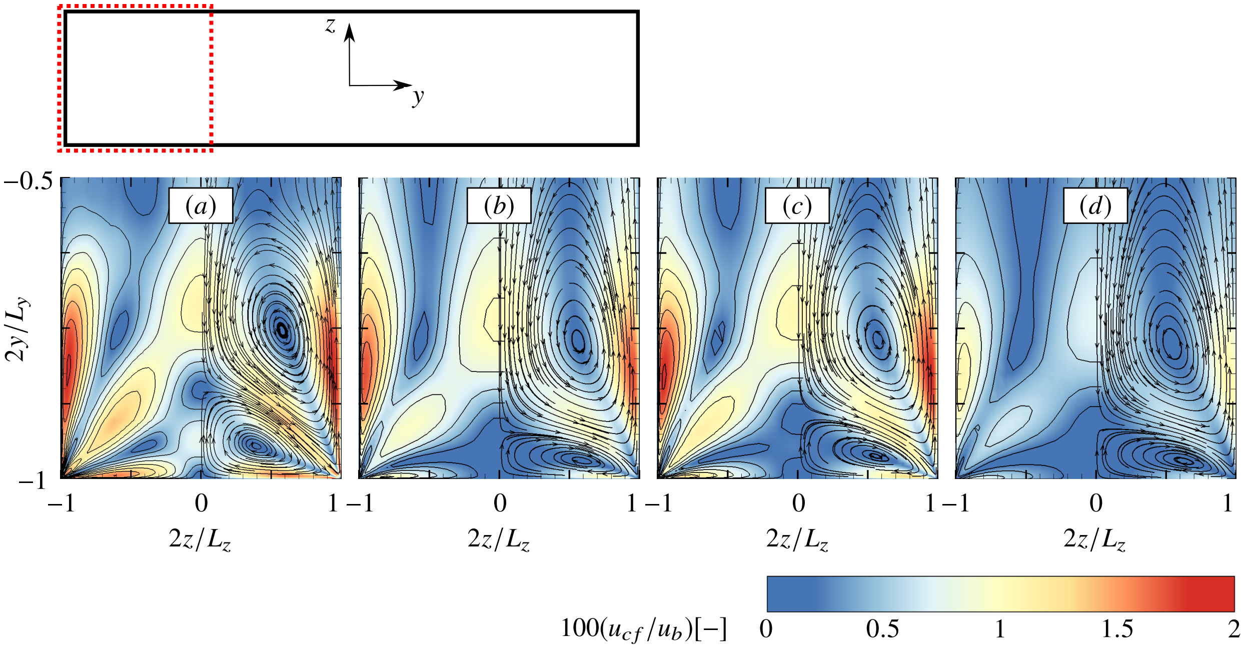

Fig. 4 Secondary flow in the lower quarter of the adiabatic HARCD for the (a) **LES, and the** (b) **BSL EARSM,** (c) **BSL RSM and** (d) **SSG RSM models. Isolines are drawn from** 0 **to** 2 **in steps of** 0.2 **and** $u_{cf} = \sqrt{v^2 + w^2}$**.**

A. Adiabatic straight duct flow field

In this section the results of the adiabatic periodic HARCD results for different RANS turbulence closure models are compared with the LES. The straight duct flow field is mainly affected by turbulence-induced secondary flow.

Due to the anisotropy of the Reynolds stress tensor in each duct corner a pair of counter-rotating vortices forms, each vortex pair spanning its entire respective duct quarter. For a square duct each vortex would possess the same size and strength. The right half of the LES flow field in figure 4 (*a*) depicts the typical turbulence-induced secondary flow structure in a HARCD, consisting of a small clockwise (CW) rotating vortex adjacent to the lower short wall and a large counter-clockwise (CCW) rotating vortex adjacent to the lateral long wall. Close to the midplane, the large CCW vortex transports fluid from the duct core towards the lower wall, then into the duct corner roughly along its bisecting line and from there is conveys fluid along the lateral side wall back towards the duct core. Again close to the duct midplane, the small CW vortex moves fluid upwards from the lower wall towards the duct core until encountering the large vortex. Then it transports fluid alongside it into the corner region and from there along the lower wall back into the wall center. This secondary flow leads to an increased mixing in the duct cross-section, i.e. an increased momentum and heat transport.

For the different RANS simulations figure 4 shows the following result: As the SST model is based on an isotropic turbulence assumption, no turbulence anisotropy can be taken into account and the turbulence-induced secondary flow is absent. All other turbulence models within this study are able to predict turbulence-induced secondary flow, although the vortex strength and location varies. The SSG RSM in figure 4 (*d*) produces the weakest cross-flow velocity, the reason being the usage of a simple wall function approach towards the wall instead of resolving the wall boundary layer. Also, the size of the small vortex is underestimated. The same observation can be made for the BSL EARSM model in figure 4 (*b*). The cross-flow velocity level is significantly higher than for the SSG RSM, although still slightly lower than for the LES. The overall best RANS results within this study are produced by the BSL RSM in figure 4 (*c*) with an increased size of the small vortices and increased u_{cf} levels. However, the small vortex size and strength is still underestimated. In the LES they extend significantly further towards the duct core, the reason being the higher ratio of small vortex strength to large vortex strength pushing the latter upwards. We attribute the weaker secondary flow throughout the RANS simulations to differences in the methodology, solver applied and wall modelling requiring further investigation. The mesh resolution can be ruled out as the RANS results are grid-converged, see appendix. The LES is based on an extensive grid convergence study and validated against DNS results, [5].

Supporting the already made observations based on the contour plots, figure 5 presents the secondary flow

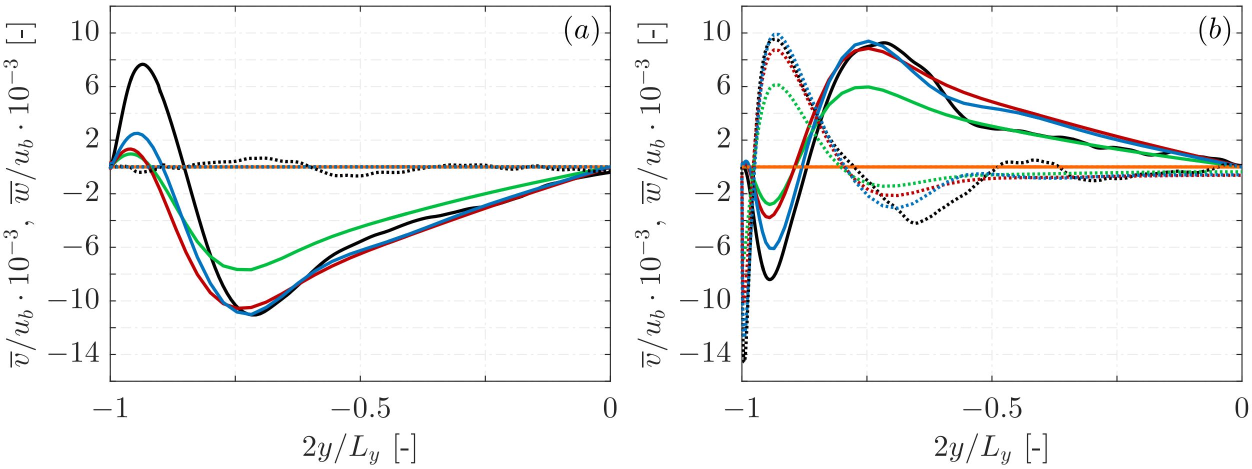

Fig. 5 Secondary flow velocity distribution along (*a*) the duct midplane $2z/L_z = 0$ and at (*b*) $2z/L_z = 0.75$ in the adiabatic HARCD for the LES (——), the SST (——), the BSL EARSM (——), the BSL RSM (——) and the SSG RSM (——). The $\overline{v}$-velocity is represented by solid and the $\overline{w}$-velocity by dotted lines.

components with the duct midplane profile in (*a*). Due to the symmetry with respect to the z-axis the $\overline{w}$-component vanishes. The $\overline{v}$-maximum represents the midplane footprint of the small vortex and the $\overline{v}$-minimum the footprint of the large vortex. We observe, that the SSG RSM strongly underestimates the strength of both the small and the large vortex. Moreover, both extremum locations are shifted towards the lower wall corresponding to the already observed vortex shift in figure 4. The BSL RSM and the BSL EARSM are both able to correctly predict the large vortex strength, but significantly underestimate the small vortex strength. The $\overline{v}$-maximum is -67.3% weaker for the BSL RSM than for the LES. However, the $\overline{v}$-maximum for the BSL EARSM is yet -46.8% lower than for the BSL RSM. Hence, the small vortex strength and size is very sensible to the chosen turbulence model. Moreover, the extremum locations are shifted towards the lower wall, although stronger for the BSL EARSM. The off-center cut in figure 5 (*b*) supports the observations made for the duct midplane, the secondary flow strength increasing from zero for the SST, over the SSG RSM, the BSL EARSM and the BSL RSM to the LES.

Figure 6 shows the dimensionless velocity profiles using the wall center friction velocity $u_{\tau,c}$ for normalization. The most prominent result is, that the SSG RSM does not resolve the wall boundary layer. All other RANS models are ω-based turbulence models and use an identical wall treatment leading to a wall-resolved result, see figure 6 (*a*). The velocity in the viscous sublayer and buffer layer is slightly underestimated compared to the LES and the analytical solution, and the slope in the logarithmic region slightly steeper. Although the latter is less prominent than for the square duct case in the appendix. The highest deviations between the different simulations occur in the outer outer layer as a consequence of the different secondary flow representation. This is especially well observable close to the lateral wall, where the vortices induce a downward kink in the u^+-profile, see figure 6 (*b*). The stronger the secondary flow, the earlier and the stronger is this downward kink, the strongest being in the LES and the weakest being in the SSG RSM. For the SST model the downward kink is absent as no secondary flow is present.

Figure 7 depicts the Reynolds stress distributions along the duct midplane. We observe, that the SSG RSM possesses the highest deviation from the LES profiles. Especially close to the wall turbulence intensity is overestimated for all components due to not resolving the wall boundary layer. None of the RANS models is able to predict the $\overline{u'u'}$-maximum in the vicinity of the lower wall underestimating streamwise turbulence intensity significantly. The same observation is made comparing RANS against DNS square duct results in the appendix. For the $\overline{v'v'}$- as well as the $\overline{w'w'}$-profiles the BSL RSM and the BSL EARSM agree sufficiently well with the LES in the log law region and the outer layer of the turbulent boundary layer, whereas the SST model overestimates the turbulence level. The Reynolds shear stress $\overline{u'v'}$ incorporates turbulent ejection and sweeping motions, the ejections from the wall being the dominant turbulent mechanism generating the secondary flow, [13]. Figure 7 (*b*) shows an overall good agreement of the $\overline{u'v'}$-component for the SST, the BSL EARSM and the BSL RSM with the LES. The upwards kink at $y+ \approx 2000$ is underestimated in the RANS simulations due to the weaker small vortex strength.

Table 2 lists the wall shear stresses and friction Reynolds numbers for the adiabatic periodic HARCD simulations.

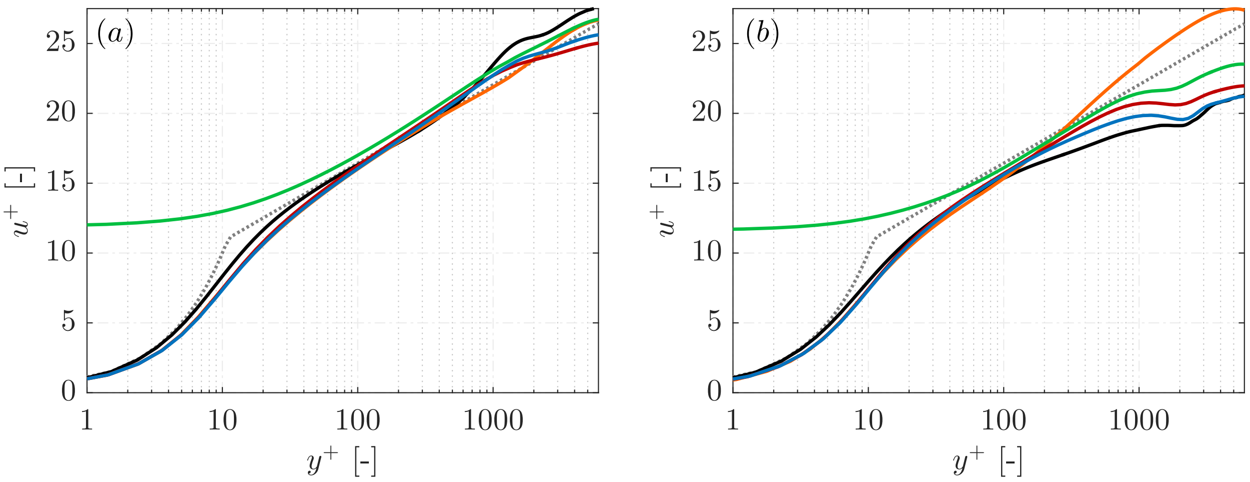

Fig. 6 Streamwise velocity distribution along (a) the duct midplane $2z/L_z = 0$ and at (b) $2z/L_z = 0.9$ in the adiabatic HARCD for the LES (———), the SST (———), the BSL EARSM (———), the BSL RSM (———) and the SSG RSM (———). The analytical law of the wall ($u^+ = 1/0.41 \cdot \ln y^+ + 5.2$) is represented by (········).

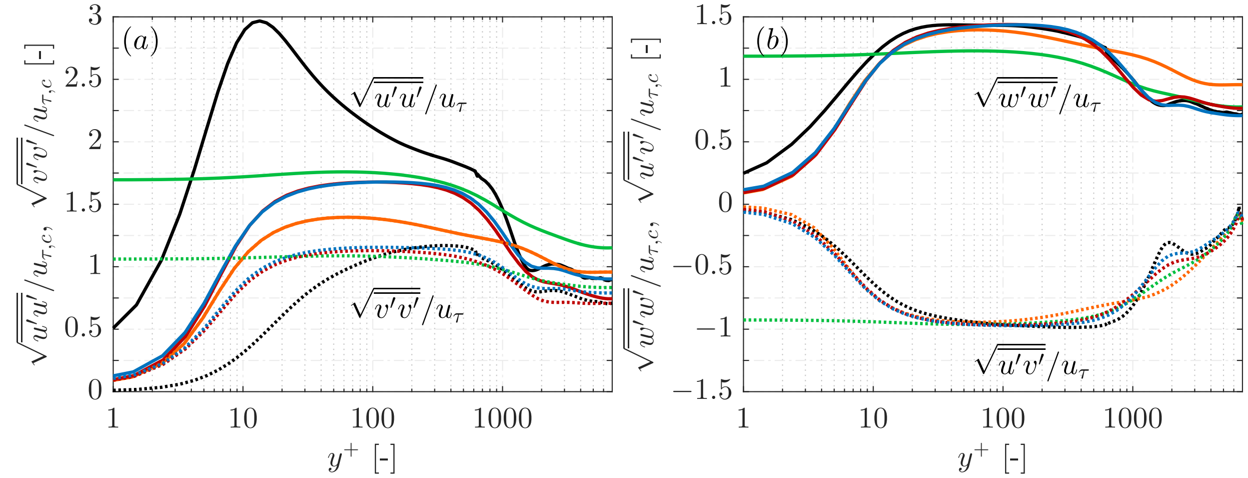

Fig. 7 Reynolds stress distributions along the duct midplane $2z/L_z = 0$ in the adiabatic HARCD for the LES (———), the SST (———), the BSL EARSM (———), the BSL RSM (———) and the SSG RSM (———). The $\overline{u'u'}$- and $\overline{w'w'}$-terms are represented by solid, and the $\overline{v'v'}$- and $\overline{u'v'}$-terms by dotted lines.

	LES	SST	BSL EARSM	BSL RSM	SSG RSM
$\tau_W\|_{y=y_{min}}$ [Pa]	53.19	47.05	54.01	54.76	49.60
$\tau_W\|_{z=z_{min}}$ [Pa]	63.93	65.08	63.09	65.74	58.72
$Re_\tau\|_{y=y_{min}}$ [-]	4778	4493	4814	4847	4613
$Re_\tau\|_{z=z_{min}}$ [-]	5238	5284	5203	5311	5020

Table 2 Wall shear stresses and friction Reynolds numbers for the different adiabatic HARCD simulations. The values represent an averaged value over the whole respective side wall.

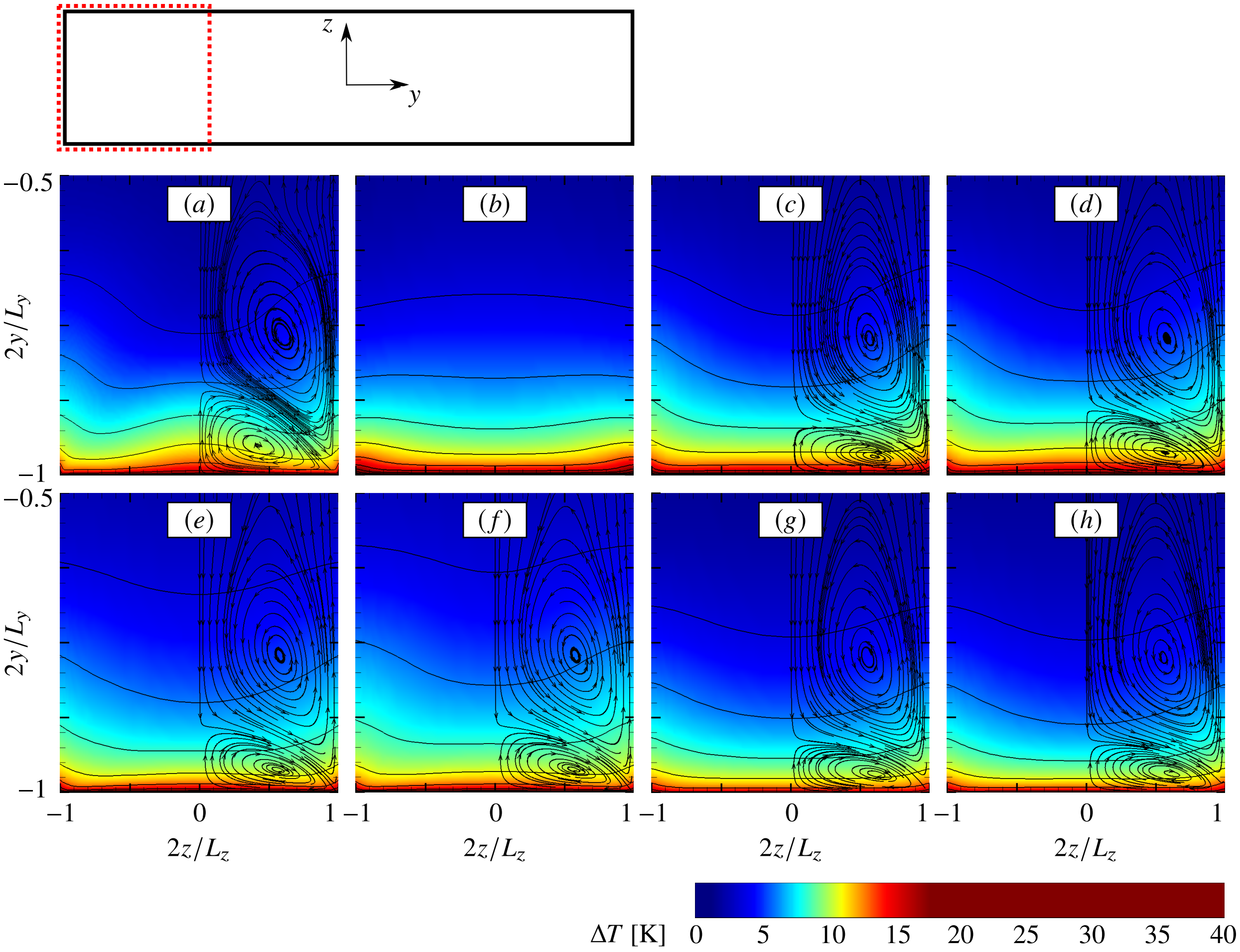

Fig. 8 Temperature increase $\Delta T = T - T_b$ in the lower HARCD quarter at $x = 500$ mm for the (a) LES, (b) SST with $Pr_t = 0.9$, (c) BSL EARSM with $Pr_t = 0.9$, (d) BSL RSM with $Pr_t = 0.9$, (e) BSL RSM with the algebraic Younis model, (f) BSL RSM with additional PDEs for $\overline{u_i'h'}$, (g) SSG RSM with $Pr_t = 0.9$ and (h) SSG RSM with the anisotropic diffusion model. Isolines are drawn from 2.5 to 40 in steps of 2.5 K.

For the SSG RSM the wall friction and the accompanying pressure loss is reduced for both the long and the short side wall compared to the ω-based RANS models and the LES. The reason is probably the differing wall treatment of the ε-based SSG RSM. The wall shear stresses for the BSL EARSM, the BSL RSM and the LES are quite similar. At the short side wall $\tau_W|_y$ is slightly overestimated in the RANS, and at the long side wall the LES value is between that of the BSL EARSM and the BSL RSM. Utilizing the SST model $\tau_W|_y$ is significantly underestimated and reduced by -11.5% compared to the LES. We attribute this observation to the missing secondary flow influence on the wall shear stress distribution of the lower wall. The long side wall is less affected by the vortex systems and consequently $\tau_W|_z$ has a similar level as the other ω-based RANS models and the LES.

B. Heated straight duct flow field

In the following we discuss the results for the heated HARCD concentrating on the location $x = 500$ mm close to the end of the straight section. In the latter only the turbulence-induced secondary flow is present becoming weaker along the duct length due to the viscosity decrease towards the heated wall. The investigation is mainly focused on the differences in the temperature profiles, turbulent heat fluxes and integral heat transfer, changes in the duct flow field are addressed briefly. The results for the RANS closure models for Reynolds stresses and turbulent heat fluxes are compared to the LES database.

In figure 8 the temperature increase ΔT within the lower duct quarter is depicted. The LES result in figure 8 (a)

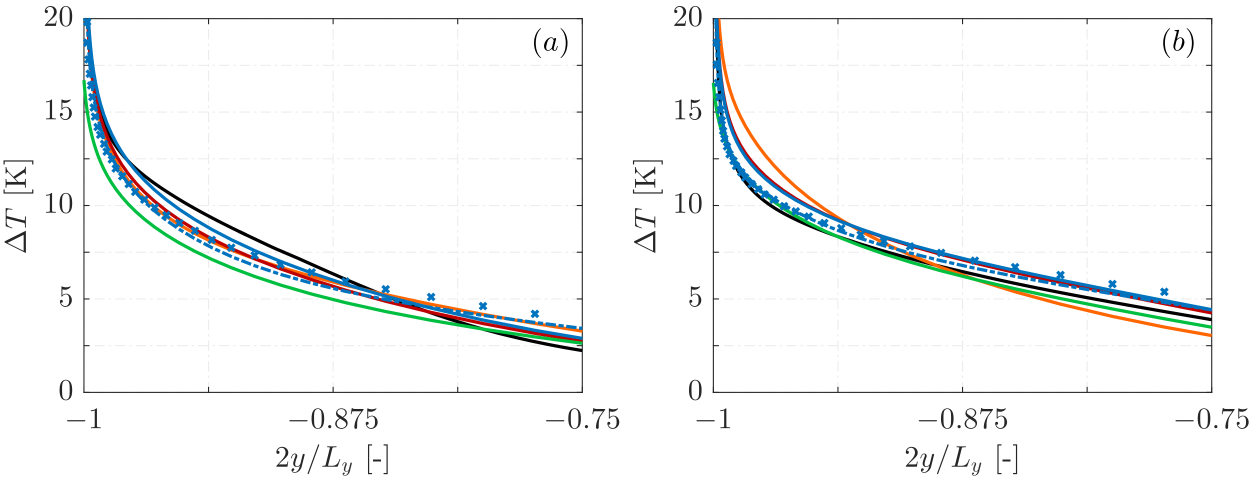

Fig. 9 Temperature increase $\Delta T = T - T_b$ at (*a*) $2z/L_z = 0$ and at (*b*) $2z/L_z = 0.9$ in the HARCD at $x = 500$ mm for the LES (——), SST with $Pr_t = 0.9$ (——), BSL EARSM with $Pr_t = 0.9$ (——), BSL RSM with $Pr_t = 0.9$ (——), BSL RSM with Younis model (-·-·-), BSL RSM with additional PDEs for $\overline{u_i'h'}$ (×) and SSG RSM with $Pr_t = 0.9$ (——).

shows the typical bent shape of the temperature profile as a consequence of the mixing of hot and cold fluid by the corner vortices. The upwards bent of the ΔT-profile in the center is caused by the small vortices and those at the lateral adiabatic walls are caused by the respective large vortex. The RANS results show several deviations for the cross-sectional temperature field: the center upwards bent above the heated wall is only visible for the BSL RSM results of figures 8 (*d*)-(*f*), although it is significantly weaker than in the LES. The reason is the underestimation of the small vortex strength in the RANS. In the LES the small vortices are substantially stronger and extend further into the duct, see section A. The upwards bent towards the lateral walls is predicted by all RANS models except for the SST in figure 8 (*b*), lacking turbulence-induced secondary flow. For the SSG RSM this upwards bent is weaker than for the BSL RSM and the BSL EARSM, compare figures 8 (*g*) with figures 8 (*c*)-(*d*). This is due to the underestimation of the large vortex strength in the SSG RSM, whereas for the BSL RSM and BSL EARSM the large vortex strength and location are in good agreement with the LES data. Focusing on how far the topmost 2.5 K-isoline penetrates into the duct core we observe, that the SSG RSM underestimates the overall heat transfer. This result is expected due to the global underestimation of the secondary flow strength. Likewise, the overall temperature level for the SST is reduced compared to the similar BSL RSM and BSL EARSM, all with $Pr_t = 0.9$, due to the lack of any secondary flow. Relevant differences between the SSG RSM with $Pr_t = 0.9$ and utilizing the anisotropic diffusion model are not visible, compare figures 8 (*g*) and (*h*). Utilizing an anisotropic turbulent heat flux closure in combination with the BSL RSM we see, that the heat transfer into the duct rises from the solution with $Pr_t = 0.9$, over the algebraic Younis-model to the BSL RSM with additional PDEs for $\overline{u_i'h'}$ due to increased turbulent mixing. The result for the less complex Daly-Harlow model (not shown) lies in between the Younis- and the PDE-result. The deviations between the BSL RSM using $Pr_t = 0.85$ (not shown) instead of $Pr_t = 0.9$ are relatively small, the heat transfer being slightly lower for the latter.

The temperature line plots of figure 9 support the contour plots of figure 8. Figure 9 (*a*) depicts the duct midplane, which is dominated by the small vortices, and figure 9 (*b*) the region close to the lateral wall, which is dominated by the large vortex. In the duct midplane $2z/L_z = 0$ we observe for all RANS models noticeable deviations from the LES distribution, which is attributed to the significantly weaker secondary flow in this area. Close to the lateral wall, the secondary flow strengths of LES and BSL RSM have a similar level, see section A. Hence, also the ΔT-profiles are in better agreement for the BSL RSM and BSL EARSM. The SST and the SSG RSM models expect significant deviations from the LES due to the underestimation or lack of secondary flow. The slope of the temperature profile towards the lower wall is improved significantly in comparison to the similar BSL RSM and BSL EARSM with $Pr_t = 0.9$ by employing the algebraic Younis model or the BSL RSM with additional PDEs. Overall the best results are achieved using the BSL RSM in combination with the Younis model. Further away from the heated wall the temperature increase is slightly overestimated, although less than using the BSL RSM/PDE-combination.

Figure 10 depicts the temperature boundary layer using dimensionless temperature profiles at the same spanwise locations as figure 9. The temperature is normalized by the friction temperature, $T^+ = T/T_\tau$ with T_τ being defined

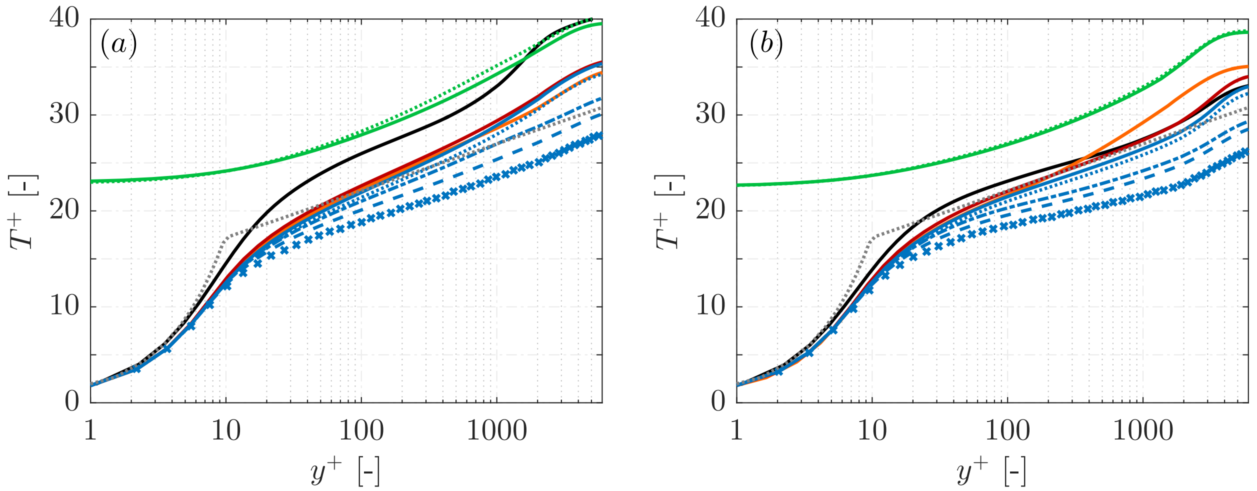

Fig. 10 Dimensionless temperature profile along (*a*) the duct midplane $2z/L_z = 0$ and at (*b*) $2z/L_z = 0.9$ in the HARCD at $x = 500$ mm for the LES (——), SST with $Pr_t = 0.9$ (——), BSL EARSM with $Pr_t = 0.9$ (——), BSL RSM with $Pr_t = 0.9$ (——), BSL RSM with $Pr_t = 0.85$ (········), BSL RSM with Daly-Harlow model (- - - -), BSL RSM with Younis model (-·-·-), BSL RSM with additional PDEs for $\overline{u_i'h'}$ (×), SSG RSM with $Pr_t = 0.9$ (——), SSG RSM with the anisotropic diffusion model (········) and the empirical function of Kader [30] (········). Normalization is performed with the local wall values at the respective spanwise location.

as $T_\tau = B_q T_W$ and the heat flux parameter as $B_q = q_W/(\rho_W\, c_{pW}\, u_\tau\, T_W)$. The empirical function of Kader [30] is defined as $T^+ = Pr\, y^+$ for the viscous sublayer and as $T^+ = 2.12\ln(y^+) + \beta(Pr)$ for the log-law region with $\beta(Pr) = (3.85Pr^{1/3} - 1.3)^2 + 2.12\ln(Pr)$. As value for Pr we utilize the wall Prandtl number of $Pr_W = 1.75$. Note, that Kader's law is derived and valid for pure channel flows without secondary flow influence assuming a constant Pr and a constant $Pr_t = 0.85$. However, for the present case, secondary flow motion is present, the turbulent Prandtl number is non-constant and varies within the cross-section, and the molecular Prandtl number varies between $Pr_W = 1.75$ and $Pr_b = 3.0$. The LES follows Kader's law in the viscous sublayer, but shows a constant upwards shift in the log-law region for figure 10 (*a*) with the profile slope fitting to that proposed by Kader's law. This is due to the mixing motion by the relatively strong small vortices, which are not present in a channel flow, and significantly weaker in the RANS. The vortices transport warmed-up fluid along the heated wall into its center leading to a local hot spot and the observed upwards shift. In figure 10 (*b*) this upwards shift almost vanishes due to a smaller secondary flow influence. As already observed for the momentum boundary layer, the SSG RSM is likewise not able to resolve the temperature boundary layer. The SST, BSL EARSM and BSL RSM, all with $Pr_t = 0.9$, behave very similar as for the momentum boundary layer, see figure 6 (*a*), as they underestimate T^+ within the viscous sublayer and possess a slightly higher slope in the log-law region. From the BSL RSM with $Pr_t = 0.9$ over $Pr_t = 0.85$ and the algebraic heat flux closure models to the BSL RSM/PDE-combination, we observe an increasing downwards shift of the temperature profile from the onset of the log-law region. Also, the profile slope is reduced. This downwards shift is accompanied by an increased global and local heat flux and consequently higher T_τ. Hence, the deviation with respect to the LES increases. Comparing the LES and the various BSL RSM results in figure 10 (*b*) support the notion, that the heat flux especially for the anisotropic heat flux closure models is overestimated.

Figure 11 compares the turbulent heat fluxes for the various RANS turbulent heat flux closure models in combination with the BSL RSM to the LES. As the $Pr_t = 0.85$ result is similar to the $Pr_t = 0.9$ result, only the latter is shown. For $Pr_t = 0.9$ the $\overline{u'T'}$-component is approximately zero at $x = 500$ mm due to the vanishing streamwise temperature gradient. The more complex heat flux closure models are able to predict a non-zero $\overline{u'T'}$-distribution. Like the $\overline{u'u'}$-peak close to the heated wall also the $\overline{u'T'}$-peak can not be reproduced by any RANS model, see section A and the appendix for comparison. The more complex algebraic Younis model represents an improvement over the Daly-Harlow model as the $\overline{u'T'}$-deviation with respect to the LES is reduced. Yet, both algebraic models underestimate the streamwise turbulent heat flux. Utilizing additional PDEs for the turbulent heat fluxes, $\overline{u'T'}$ is overestimated in the midplane. Close to the lateral wall the conclusions are similar as for the midplane, though the deviations from the LES further away from the heated wall are significantly smaller. The heated wall-normal turbulent heat flux $\overline{v'T'}$ is overestimated by

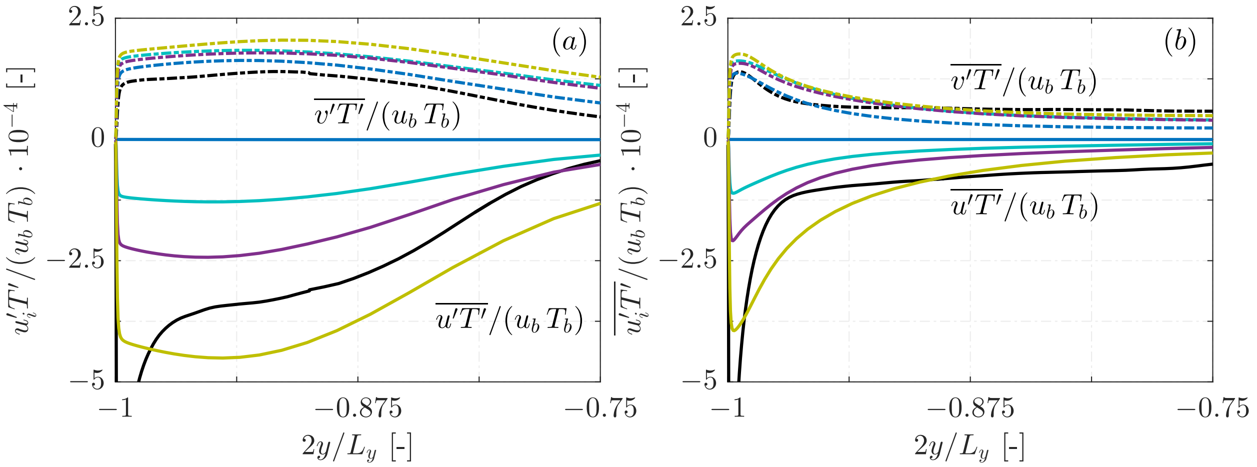

Fig. 11 Turbulent heat fluxes $\overline{u_i'T'}$ at (a) $2z/L_z = 0$ and at (b) $2z/L_z = 0.9$ in the HARCD at $x = 500$ mm for the LES (——), BSL RSM with $Pr_t = 0.9$ (——), BSL RSM with Daly-Harlow model (——), BSL RSM with Younis model (——) and BSL RSM with additional PDEs for $\overline{u_i'h'}$ (——). $\overline{u'T'}$ is represented by solid lines and $\overline{v'T'}$ by dash-dotted lines.

	straight duct 0 – 500 mm	curved duct	total configuration
LES	3.20		
SST, $Pr_t = 0.9$	3.28	0.58	4.45
BSL EARSM, $Pr_t = 0.9$	3.48	0.60	4.70
SSG RSM, $Pr_t = 0.9$	3.00	0.50	4.05
SSG RSM, anisotropic	2.96	0.49	4.00
BSL RSM, $Pr_t = 0.85$	3.69 (+2.8%)	0.62 (+1.6%)	4.97 (+2.5%)
BSL RSM, $Pr_t = 0.9$	3.59 (+0.0%)	0.61 (+0.0%)	4.85 (+0.0%)
BSL RSM, Daly-Harlow model	4.07 (+13.4%)	0.66 (+8.2%)	5.47 (+12.8%)
BSL RSM, Younis model	3.90 (+8.6%)	0.64 (+4.9%)	5.25 (+8.2%)
BSL RSM, PDE	4.35 (+21.2%)	0.70 (+14.8%)	5.84 (+20.4%)

Table 3 Integral heat fluxes $\dot{Q}$ for the different HARCD simulations.

all employed RANS heat flux models giving a possible explanation for the higher overall heat transfer into the duct compared to the LES, see table 3. The $\overline{w'T'}$-distribution is not explicitly shown as it is zero in the midplane due to the symmetry. Close to the lateral wall it follows a similar trend as $\overline{v'T'}$, although with a lower magnitude.

The integral heat fluxes in the left column of table 3 support the observations made based on the temperature distributions within the current section: The SSG RSM with $Pr_t = 0.9$ as well as with the usage of the anisotropic diffusion model both underestimate the heat transfer, even though secondary flow is present. This deviation is attributed to the wall treatment of the ε-based model, not resolving the turbulent boundary layer. The SST simulation gives a slightly higher integral heat flux than the LES. This result is not to be expected due to the lack of turbulence-induced secondary flow and consequently a weaker mixing of hot and cold fluid. We attribute this behavior to a possible overestimation of the wall heat flux due to the automatic wall treatment option of ANSYS CFX. When turbulence-induced secondary flow is present, as in the BSL EARSM result, the mixing and with it the overall heat transfer is augmented with respect to the SST. With the higher secondary flow strength in the BSL RSM result with $Pr_t = 0.9$ the integral heat flux grows further. Modifying $Pr_t = 0.9$ to $Pr_t = 0.85$ further increases the integral heat flux as well as utilizing more sophisticated turbulent heat flux closure models, from the Younis over the Daly-Harlow model to the BSL RSM/PDE combination. The latter predicts the strongest heat transfer being over 20% higher than that of the standard BSL RSM

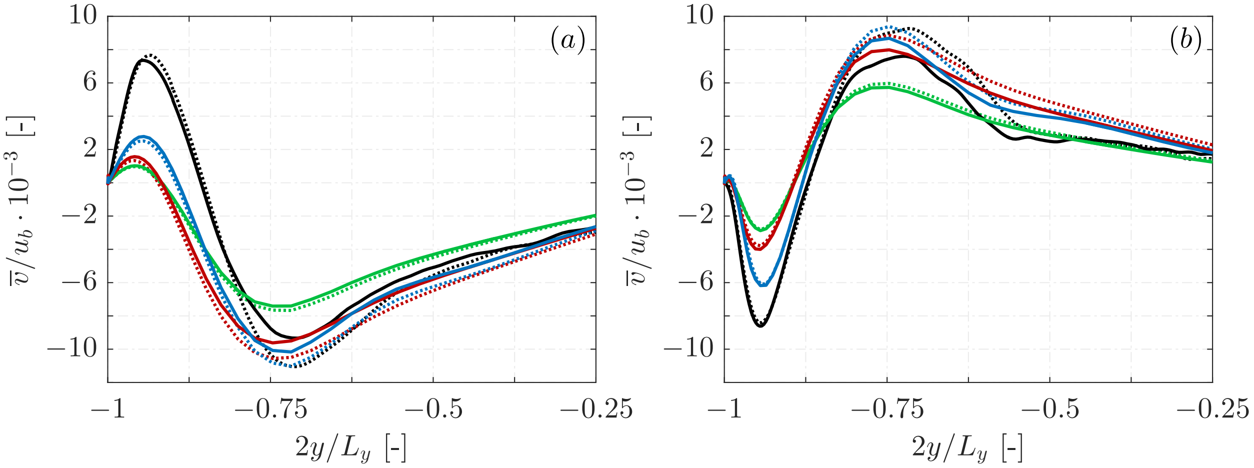

Fig. 12 Secondary flow distribution at (a) $2z/L_z = 0$ and at (b) $2z/L_z = 0.75$ in the HARCD at $x = 500$ mm for the LES (——), the BSL EARSM with $Pr_t = 0.9$ (——), the BSL RSM with $Pr_t = 0.9$ (——) and the SSG RSM with $Pr_t = 0.9$ (——). The respective adiabatic HARCD results are represented by dotted lines.

	$\tau_W\|_{y=y_{min}}$ [Pa]	$\tau_W\|_{z=z_{min}}$ [Pa]	$Re_\tau\|_{y=y_{min}}$ [-]	$Re_\tau\|_{z=z_{min}}$ [-]
LES	45.74 (−14.0%)	64.57 (+1.0%)	7205 (+50.8%)	5264 (+0.5%)
SST, $Pr_t = 0.9$	43.71 (−7.1%)	64.83 (−0.4%)	7043 (+56.8%)	5274 (−0.2%)
BSL EARSM, $Pr_t = 0.9$	49.69 (−8.0%)	62.87 (−0.3%)	7510 (+56.0%)	5194 (−0.2%)
SSG RSM, $Pr_t = 0.9$	47.83 (−3.6%)	58.60 (−0.2%)	7368 (+59.7%)	5015 (−0.1%)
SSG RSM, anisotropic	47.79 (−3.6%)	58.60 (−0.2%)	7365 (+59.6%)	5015 (−0.1%)
BSL RSM, $Pr_t = 0.85$	51.00 (−6.9%)	65.45 (−0.4%)	7608 (+56.9%)	5299 (−0.2%)
BSL RSM, $Pr_t = 0.9$	50.96 (−6.9%)	65.44 (−0.5%)	7605 (+56.9%)	5299 (−0.2%)
BSL RSM, Daly-Harlow model	51.06 (−6.8%)	65.43 (−0.5%)	7612 (+57.0%)	5298 (−0.2%)
BSL RSM, Younis model	51.03 (−6.8%)	65.43 (−0.5%)	7610 (+57.0%)	5299 (−0.2%)
BSL RSM, PDE	51.13 (−6.6%)	65.42 (−0.5%)	7618 (+57.2%)	5298 (−0.2%)

Table 4 Wall shear stresses and friction Reynolds numbers at $x = 500$ mm for the HARCD simulations, and relative change with respect to the adiabatic case. The values are averaged over the whole respective side wall.

with $Pr_t = 0.9$. Hence, compared to the LES a significant overestimation of the turbulent heat flux is present. Note, that modelling $\overline{u_i'h'}$ with additional PDEs is still a beta feature within ANSYS CFX. The wall shear stresses of the BSL EARSM and BSL RSM model combinations are likewise overestimated in the RANS, see table 4. This result is expectable due to the Reynolds analogy proposing the proportionality $\dot{q}_W \propto \tau_W$.

The heating and associated viscosity reduction towards the lower wall leads to a weakening of the turbulent fluctuations, reduced wall shear stresses and a reduction of the secondary flow strength along the duct, [5]. Figure 12 (a) shows exemplarily the reduction of the secondary flow strength in the midplane using the $\overline{v}$-component. In the LES we observe the expected shift of the small vortex towards the heated wall and a slight reduction of its strength. The $\overline{v}$-minimum of the large vortex is reduced noticeable and its position remains approximately constant. The RANS results show similar tendencies for the large vortex, although the secondary flow strength reduction is weaker. Surprisingly the small vortex strength increases in the duct midplane. At the off-center location similar tendencies are visible for the large vortex and the small vortex strength increases slightly for all considered simulations. Comparing the wall shear stresses in table 4, we observe a significantly stronger drop in the LES with −14% as in the ω-based RANS models with $\approx -7\%$, further increasing the deviation from the LES. Likewise the deviation in $Re_\tau|_{y=y_{min}}$ increases further. The lateral wall shear stress is only slightly affected by the heating as an average value over the whole side wall is considered.

C. Heated curved duct flow field

In the current section the secondary flow and temperature field within the curved part of the HARCD is discussed for the different RANS turbulence closure model combinations. Currently no LES results are available for comparison. The discussion focuses on the end cross-section of the 90°-bend, where the pressure-induced secondary flow is fully developed.

The typical secondary flow structure is shown in figure 13 (j). The curvature-induced centrifugal force, respectively the radial pressure gradient, leads to a significant momentum and temperature redistribution in the duct cross-section. From the beginning of the curved section Prandtl's flow of the first kind forms, superimposing the an order of magnitude weaker Prandtl's flow of the second kind having formed upstream along the straight section. The secondary flow field consists of two large counter-rotating vortices, the so-called Dean vortices, spanning the whole cross-section. Each is accompanied by a small vortex in the vicinity of the heated wall corner with the same direction of rotation. Turbulence anisotropy as the source of turbulence-induced secondary flow is still present, but plays a minor role. The situation is different with a weaker curvature or at the start of the curved section. There the secondary flow strengths can have a similar order of magnitude. Focusing on the lower half of figure 13 (j), i.e. the clockwise rotating Dean vortex, cold fluid from the duct core is transported along the lateral wall towards the lower heated wall. In the corner region the small vortex mixes it with warmed-up fluid. The Dean vortex continues by conveying heated fluid from the duct corner along the heated wall into its center and from there upwards into the duct core. These strong mixing motions by both Dean and accompanying small vortices create a spearhead- or candle flame-shaped temperature distribution. By transporting cold fluid towards the heated wall and warmed-up fluid away from it into the duct core, the Dean vortices are able to significantly increase heat transfer by ensuring an augmented wall temperature gradient.

The left column of figure 13 shows, that all RANS simulations are able to predict the pressure-induced secondary flow and that the differences between the turbulence models are less prominent than for the straight duct investigation. As the chosen heat flux closure model does not visibly affect the secondary flow fields, only those for the $Pr_t = 0.9$ configurations are explicitly shown. We observe, that for the SST model the Dean vortex core is shifted towards the upper wall in comparison to the other turbulence models. Moreover, the cross-sectional velocity for the SST is higher in the duct core as well as along the lateral walls indicating stronger Dean vortices. Comparing the SST with the highest u_{cf} in the duct core, i.e. at $2y/L_y = 0$ and $2z/L_z = 0$, u_{cf} for the BSL EARSM is by $\approx 11\%$ smaller and the lowest. However, the BSL EARSM has an increased u_{cf} towards the heated wall missing the droplet-shaped low-velocity region around $2z/L_z = 0$ and between $2y/L_y = -0.9$ and -0.7, which is visible for all other models. The small vortex located in the heated wall duct corner is strongest and largest in the SSG RSM followed by the BSL RSM and weaker in the other two models. Especially in the BSL EARSM is appears to be rather weak and flattened. We attribute the deviations in the cross-sectional flow on the ability of the turbulence model to account for turbulence anisotropy in two ways: on the one hand the corner vortices have already formed upstream of the bend and on the other hand turbulence-induced secondary flow is still forming along the bend, both interacting with the pressure-induced secondary flow.

The right column of figure 13 shows, that all temperature profiles possess the typical spearhead-shaped form. First we compare the different turbulence models with $Pr_t = 0.9$. The SSG RSM of figure 13 (k) has a visibly lower temperature level than the other three. The BSL RSM and BSL EARSM ΔT-profiles, figures 13 (d) and (f), are broader especially in the vicinity of the lower wall than the SST in figure 13 (b). The SST possesses a lense-shaped spearhead-maximum, whereas the BSL RSM has a droplet-shaped one and the BSL EARSM result lies in between. Comparing the SSG RSM results of figures 13 (k) and (l) shows, that the anisotropic diffusion model leads to a slightly increased temperature diffusion predicting a reduced spearhead-maximum. Comparing the different turbulent heat flux closure models in combination with the BSL RSM of figures 13 (f), (g), (h) and (i) we observe, that the $Pr_t \neq const.$ anisotropic models predict a significant broadening of the temperature-profile and reduction of the spearhead-maximum. Hence, they predict an increased mixing of hot and cold fluid and a higher overall heat transfer. The mixing increases from the $Pr_t = 0.9$ solution over the algebraic, relatively simple Daly-Harlow model and the more complex Younis-model to the case using additional PDEs for the turbulent heat fluxes. The latter predicts a deeper penetration of the heated fluid in heated wall-normal direction, the 2 K-isoline reaching the duct core. Consequently, the BSL RSM with additional PDEs for $\overline{u_i'h'}$ predicts the highest heat transfer into the flow. The solution for $Pr_t = 0.85$ (not depicted) has no major deviations from the $Pr_t = 0.9$ result except for a slight broadening of the temperature profile close to the heated wall.

The observations made for the contour plots are supported by the tabulated integral heat fluxes along the bend, see table 3. Both SSG RSM underestimate $\dot{Q}$, whereas the heat fluxes for the SST, BSL EARSM and BSL RSM with $Pr_t = 0.9$ are similar. Modelling the turbulent heat flux as anisotrop leads, as already observed, to an improved mixing and overall higher heat transfer into the flow. For example, the integral heat flux over the curved section for the BSL RSM with additional PDEs is $\approx 15\%$ higher than that of the BSL RSM with $Pr_t = 0.9$.

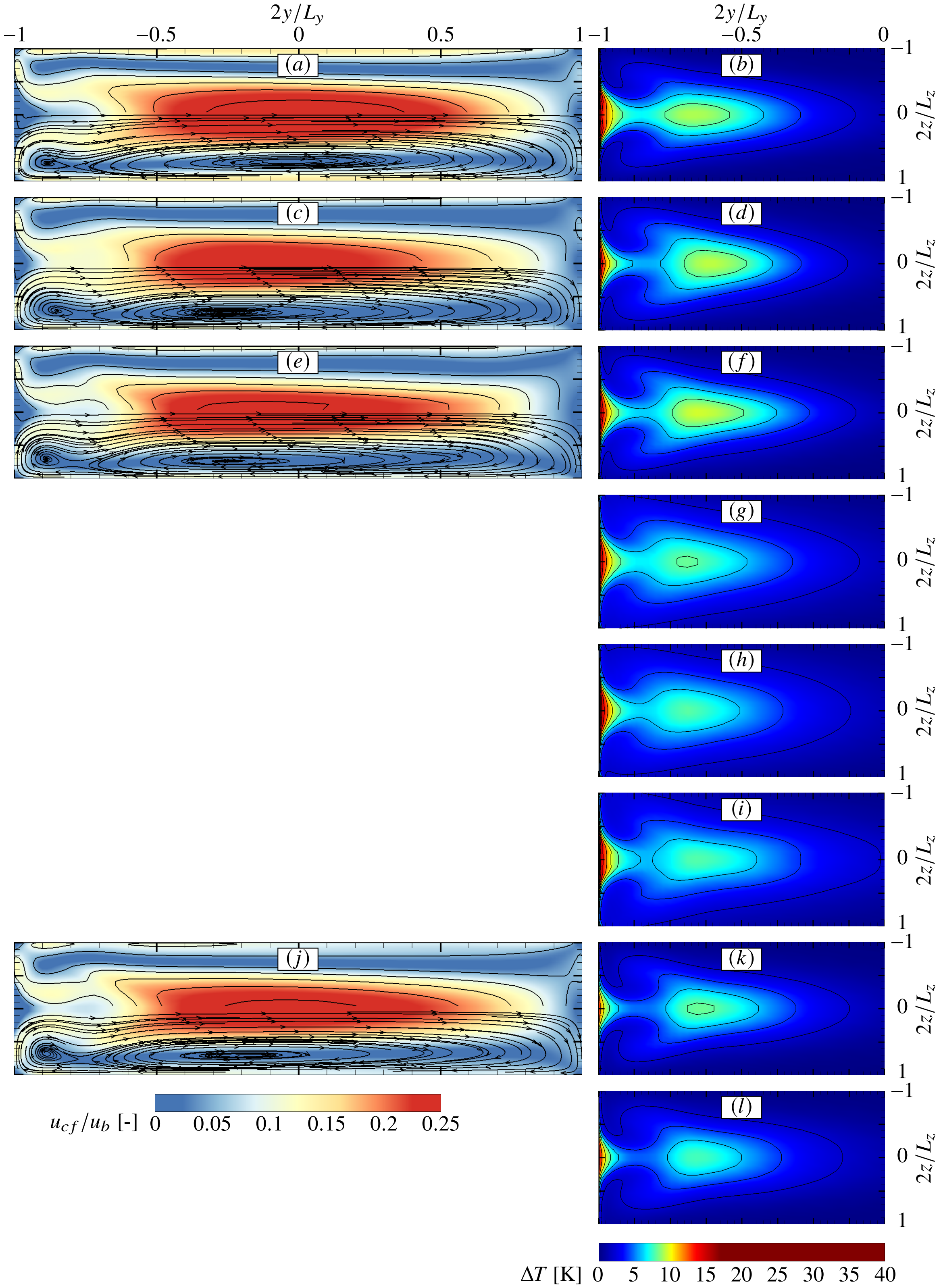

Fig. 13 Secondary flow $u_{cf} = \sqrt{u^2 + w^2}$ and temperature increase $\Delta T = T - T_b$ at the outlet of the heated bend for the (a)/(b) SST with $Pr_t = 0.9$, (c)/(d) BSL EARSM with $Pr_t = 0.9$, (e)/(f) BSL RSM with $Pr_t = 0.9$, (g) BSL RSM with the algebraic Daly-Harlow model, (h) BSL RSM with the algebraic Younis model, (i) BSL RSM with additional PDEs for $\overline{u_i' h'}$, (j)/(k) SSG RSM with $Pr_t = 0.9$ and (l) SSG RSM with the anisotropic diffusion model. Isolines are drawn from 0 to 0.25 in steps of 0.05 for u_{cf} and from 2 to 40 in steps of 2 for ΔT.

V. Summary and Conclusion

We have presented the results for well-resolved RANS simulations of a generic HARCD configuration at $Re_b = 110 \times 10^3$ with an asymmetrical wall heating at a constant $\Delta T = T_W - T_b = 40\,\mathrm{K}$. The setup consists of three parts: the periodic adiabatic feed line, the straight heated section and a heated 90° bend at the end. Utilizing the first we analysed the prediction capabilities of turbulence-induced secondary flow, utilizing the second we investigated the interaction of secondary flow and turbulent heat transfer, and utilizing the third we discussed the interaction of pressure- and turbulence-induced secondary flow and the resulting temperature field. For the RANS simulations we selected several turbulence closure models for Reynolds stresses and turbulent heat fluxes available within ANSYS CFX, respectively added them using algebraic models. The various RANS results for the adiabatic and the heated straight duct have been thoroughly compared against the well-resolved LES database by Kaller et al. [5].

Due to turbulence anisotropy a relatively weak secondary flow forms in the straight duct, manifesting itself as a pair of a small and a large counter-rotating vortex in each duct corner. As the SST model is based on an isotropic turbulence closure assumption, turbulence-induced secondary flow can not be represented. The SSG RSM is able to account for turbulence anisotropy, but the vortex strength is significantly underestimated. The reason is, that the ε-based SSG RSM model does not resolve the turbulent boundary layer, leading to a misrepresentation of turbulence and velocity profiles towards the walls. For the BSL RSM and BSL EARSM the strength and location of the large vortex at the lateral wall agrees well with the LES. However the strength and extension of the small vortex above the heated wall is significantly underestimated, the deviation of the BSL EARSM being higher. In both models the wall shear stress for the short heatable wall is overestimated slightly. The ω-based turbulence models show deficiencies predicting the Reynolds stresses towards the wall, especially the streamwise $\overline{u'u'}$-peak is significantly underestimated compared to the HARCD LES as well as the square duct DNS by Pirozzoli et al. [17]. The overall best agreement with LES data is achieved by employing the BSL RSM model followed by the BSL EARSM model.

All RANS models show noticeable deviations from the LES temperature profile in the heated duct midplane. The reason are the significantly stronger small vortices, which transport warmed-up fluid above the heated wall into its center creating a hot spot. The latter is only captured using the BSL RSM model, but less prominent. The SSG RSM predicts the lowest overall heat transfer, the reason being not resolving the turbulent boundary layer and the weak secondary flow. Using the anisotropic diffusion model for turbulent heat flux closure in combination with the SSG RSM instead of a constant $Pr_t = 0.9$ does not alter the result visibly. Surprisingly, the SST model with $Pr_t = 0.9$ predicts a similar integral heat flux as the LES, although lacking any mixing by the secondary flow. We attributed this result to the usage of the so-called automatic wall treatment option for ω-based models by ANSYS CFX. Consequently, utilizing the related BSL EARSM with $Pr_t = 0.9$ leads to a heat transfer rise due to the presence of turbulence-induced secondary flow. Employing various turbulent heat flux closure models in combination with the BSL RSM showed, that the temperature profile towards the wall for the $Pr_t = 0.9$ standard model combination can be improved by using the algebraic Younis model or additional PDEs for $\overline{u_i'h'}$. However, the overall heat transfer rises further increasing the deviation with respect to the LES. A possible explanation is the overestimation of the heated wall-normal turbulent heat flux component $\overline{v'T'}$, observed for all BSL RSM model combinations. As for the integral heat flux, the deviation increases further from the $Pr_t = 0.9$ option over employing the algebraic Younis and Daly-Harlow model to the usage of additional PDEs. Similarly the wall shear stress at the heated wall is overestimated and the deviation with respect to the LES higher than for the adiabatic duct. Overall we observed the surprising result, that the more sophisticated the employed RANS model combination, the higher the overestimation of the integral heat transfer. This motivates further investigation.

Along the curved section the stronger pressure-induced secondary flow forms due to centrifugal forces, superimposing the significantly weaker turbulence-induced one. The cross-sectional flow field is dominated by the two large counter-rotating Dean vortices spanning the whole duct cross-section, which all RANS models are able to predict. The specific choice of turbulence model combination has still a noticeable impact on the resulting secondary flow and temperature field due to the different prediction capabilities for the upstream flow field in the straight section, for turbulence-anisotropy within the bend, and for the turbulent heat fluxes. LES data for comparison of the curved duct results is currently not available.

Appendix

To assess the accuracy of the present HARCD RANS simulation, we additionally performed a RANS for an adiabatic square duct with an edge length of $2h$ at $Re_b = 40 \cdot 10^3$ and $Re_\tau = 1055$, case D of Pirozzoli et al. [17].

The RANS grid for this comparison follows the resolution used in our investigation of the HARCD at $Re_b = 110 \cdot 10^3$, i.e. comparable x^+, y^+ and z^+ are employed. Additionally a RANS at a finer grid resolution has been performed to show

	Re_b	$Re_{\tau,c}$	$u_{\tau,c}$ [m/s]	l_c^+ [m]	x^+	y^+/z^+	$\frac{\Delta y_{max}}{\Delta y_{min}}$ / $\frac{\Delta z_{max}}{\Delta z_{min}}$	$N_x \times N_y \times N_z$
$RANS$	$40 \cdot 10^3$	1006	0.048	$9.94 \cdot 10^{-6}$	718.25	1.00	52.5	$21 \times 83 \times 83$
$RANS(fine)$	$40 \cdot 10^3$	1009	0.048	$9.91 \cdot 10^{-6}$	236.50	1.01	34.01	$64 \times 192 \times 192$
LES	$40 \cdot 10^3$	1089	0.052	$9.18 \cdot 10^{-6}$	65.33	1.06	23.41	$378 \times 138 \times 138$
DNS	$40 \cdot 10^3$	1073	0.051	$9.32 \cdot 10^{-6}$				

Table 5 Main flow and grid parameters for the RANS-LES-DNS comparison for the square duct simulation. The index c stands for the wall center value at $z = 0$

grid convergence. Both simulations are performed using the BSL RSM turbulence model. The grid and simulation parameters for the square duct comparison of DNS, LES and RANS results are listed in table 5. The streamwise box length is chosen to $7.5\,d_h$. The temporal averaging for the LES is performed over 200 FTT with respect to the streamwise box length. Additionally, a spatial averaging in streamwise direction is applied for the LES.

Figure 14 compares the RANS with the LES and the DNS results. To normalize the streamwise velocity and Reynolds stresses the center friction velocity $u_{\tau,c}$ is used, and for the secondary flow components the bulk velocity u_b. The RANS results for the utilized resolution are grid-converged as the comparison with the fine resolution RANS shows. The streamwise velocity profile possesses a steeper inclination in the logarithmic region of the boundary layer compared to the DNS, the LES and the analytical law of the wall. Note, that for the HARCD at a similar grid resolution the inclination is less steep. The secondary flow strength and location of the vortices is with only slight deviations in good agreement with DNS and LES data. For the turbulent Reynolds stresses, the shear stress term $\overline{u'v'}$ agrees well with the DNS results, however, the normal turbulent stresses $\overline{u'u'}$, $\overline{v'v'}$, $\overline{w'w'}$ show major deviations from both DNS and LES. To rule out any setup errors, we performed several modifications of the test case including the usage of the BSL EARSM turbulence model and simulating a very long spatially resolved straight square duct with the fluid being treated both incompressible and compressible, however, the observed deviations persisted. Table 5 shows, that the friction Reynolds number in the wall center $Re_{\tau,c}$ is underestimated within the RANS simulations. This is due to a stronger drop of the wall shear stress distribution in the wall center compared to the DNS and LES.

Acknowledgments

Financial support has been provided by the German Research Foundation (Deutsche Forschungsgemeinschaft – DFG) within the framework of the Sonderforschungsbereich Transregio 40, SFB-TRR40 (Technological foundations for the design of thermally and mechanically highly loaded components of future space transportation systems). Computational resources have been provided by the Leibniz Supercomputing Centre Munich (LRZ).

References

[1] Demuren, A. O., and Rodi, W., "Calculation of turbulence-driven secondary motion in non-circular ducts," *Journal of Fluid Mechanics*, Vol. 140, 1984, pp. 189–222.

[2] Salinas-Vásquez, M., and Métais, O., "Large-eddy simulation of the turbulent flow through a heated square duct," *Journal of Fluid Mechanics*, Vol. 453, 2002, pp. 201–238.

[3] Kays, W. M., "Turbulent Prandtl Number - Where Are We?" *Journal of Heat Transfer*, Vol. 116, No. 2, 1994, pp. 284–295.

[4] Hirota, M., Fujita, H., Yokosawa, H., Nakai, H., and Itoh, H., "Turbulent heat transfer in a square duct," *International Journal of Heat and Fluid Flow*, Vol. 18, No. 1, 1997, pp. 170–180.

[5] Kaller, T., Pasquariello, V., Hickel, S., and Adams, N. A., "Turbulent flow through a high aspect ratio cooling duct with asymmetric wall heating," *Journal of Fluid Mechanics*, Vol. 860, 2019, pp. 258–299.

[6] Daly, B. J., and Harlow, F. H., "Transport equations in turbulence," *Physics of Fluids*, Vol. 13, No. 11, 1970, pp. 2634–2649.

[7] Younis, B. A., Speziale, C. G., and Clark, T. T., "A rational model for the turbulent scalar fluxes," *Proceedings of the Royal Society A: Mathematical, Physical and Engineering Sciences*, Vol. 461, No. 2054, 2005, pp. 575–594.

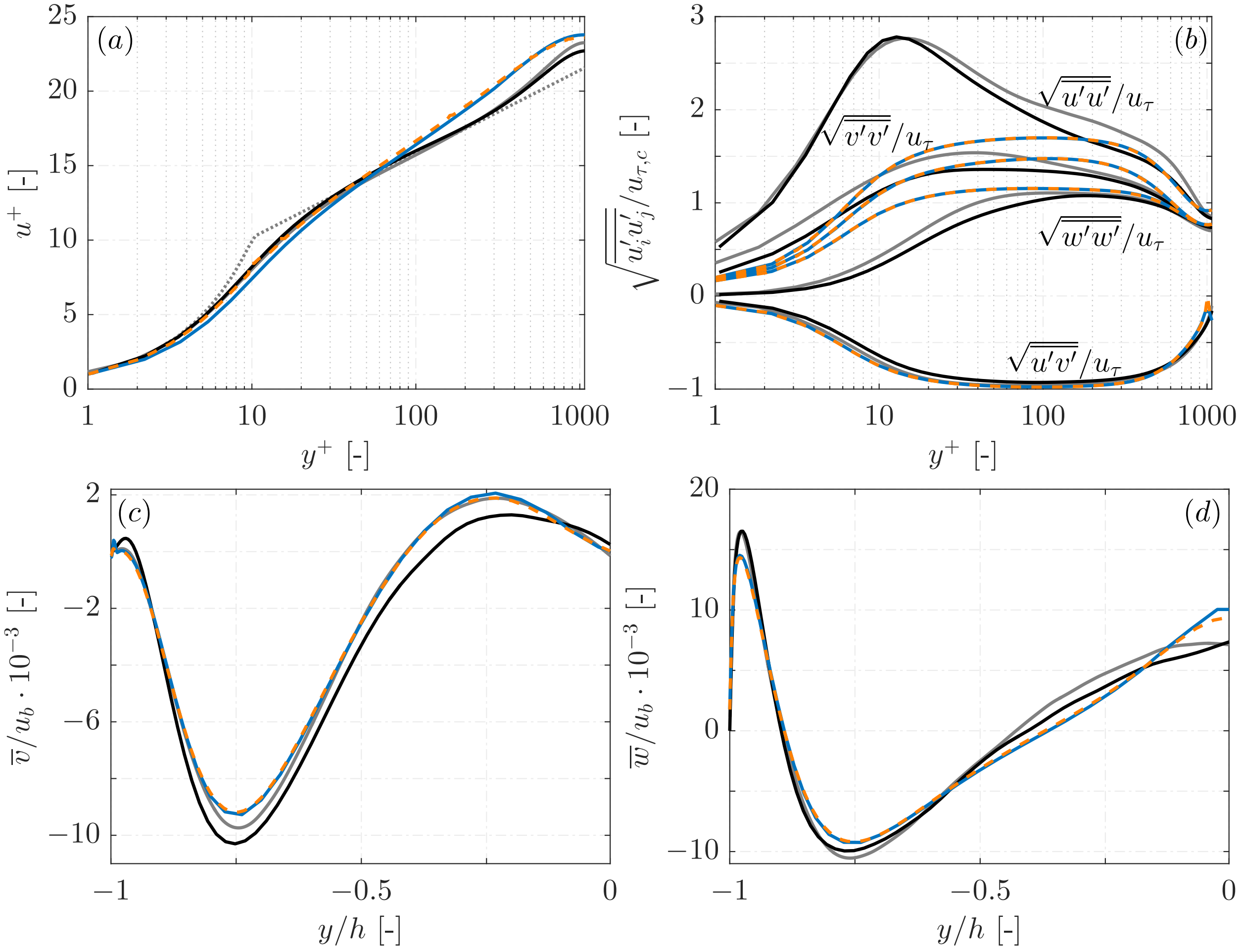

Fig. 14 Profiles of (a) **mean streamwise velocity and** (b) **Reynolds stresses along the duct midplane at** $z = 0$**, and** (c)**/**(d) **secondary flow velocities at** $z/h = 0.75$ **for the LES (——), the DNS (——), the RANS at production resolution (——) and the RANS at the finest grid resolution (- - - -) for the adiabatic square duct simulation. In** (a) **the analytical law of the wall (**$u^+ = 1/0.41 \cdot \ln y^+ + 4.55$**) is represented by (········).**

[8] Rochhausen, S., “Modellierung des turbulenten Wärmeflusses in Turbomaschinenströmungen,” Ph.D. thesis, Ruhr-Universität Bochum, 2017.

[9] Baines, W. D., and Brundrett, E., “The production and diffusion of vorticity in duct flow,” *Journal of Fluid Mechanics*, Vol. 19, 1964, pp. 375–394.

[10] Gessner, F. B., and Jones, J. B., “On some aspects of fully-developed turbulent flow in rectangular channels,” *Journal of Fluid Mechanics*, Vol. 23, No. 4, 1965, pp. 689–713.

[11] Monty, J. P., “Developments In Smooth Wall Turbulent Duct Flows,” Ph.D. thesis, The University of Melbourne, 2005.

[12] Gavrilakis, S., “Numerical simulation of low-Reynolds-number turbulent flow through a straight square duct,” *Journal of Fluid Mechanics*, Vol. 244, 1992, pp. 101–129.

[13] Huser, A., and Biringen, S., “Direct numerical simulation of turbulent flow in a square duct,” *Journal of Fluid Mechanics*, Vol. 257, 1993, pp. 65–95.

[14] Madabhushi, R. K., and Vanka, S. P., “Large eddy simulation of turbulence-driven secondary flow in a square duct,” *Physics of Fluids A: Fluid Dynamics*, Vol. 3, No. 11, 1991, pp. 2734–2745.

[15] Vinuesa, R., Noorani, A., Lozano-Duran, A., El Khoury, G., Schlatter, P., Fischer, P. F., and Nagib, N. M., “Aspect ratio effects in turbulent duct flows studied through direct numerical simulation,” *Journal of Turbulence*, Vol. 15, No. 10, 2014, pp. 677–706.

[16] Choi, H. S., and Park, T. S., “The influence of streamwise vortices on turbulent heat transfer in rectangular ducts with various aspect ratios,” *International Journal of Heat and Fluid Flow*, Vol. 40, 2013, pp. 1–14.

[17] Pirozzoli, S., Modesti, D., Orlandi, P., and Grasso, F., “Turbulence and secondary motions in square duct flow,” *Journal of Fluid Mechanics*, Vol. 840, 2018, pp. 631–655.

[18] Pizzarelli, M., Nasuti, F., and Onofri, M., “Numerical Analysis of Three-Dimensional Flow of Supercritical Fluid in Asymmetrically Heated Channels,” *AIAA Journal*, Vol. 47, No. 11, 2009, pp. 2534–2543.

[19] Pizzarelli, M., Nasuti, F., and Onofri, M., “Analysis of Curved-Cooling-Channel Flow and Heat Transfer in Rocket Engines,” *Journal of Propulsion and Power*, Vol. 27, No. 5, 2011, pp. 1045–1053.

[20] Pizzarelli, M., Nasuti, F., and Onofri, M., “Trade-off analysis of high-aspect-ratio-cooling-channels for rocket engines,” *International Journal of Heat and Fluid Flow*, Vol. 44, 2013, pp. 458–467.

[21] Rochlitz, H., Scholz, P., and Fuchs, T., “The flow field in a high aspect ratio cooling duct with and without one heated wall,” *Experiments in Fluids*, Vol. 56, No. 12, 2015, pp. 1–13.

[22] Rochlitz, H., and Scholz, P., “Application of laser-induced fluorescence technique in a duct flow with one heated wall,” *Experiments in Fluids*, Vol. 59, No. 3, 2018.

[23] Kaller, T., Pasquariello, V., Hickel, S., and Adams, N., “Large-eddy simulation of the high-Reynolds-number flow through a high-aspect-ratio cooling duct,” *Proceedings of the 10th International Symposium on Turbulence and Shear Flow Phenomena (TSFP-10), Chicago*, 2017.

[24] Kaller, T., Hickel, S., and Adams, N., “LES of an Asymmetrically Heated High Aspect Ratio Duct at High Reynolds Number at Different Wall Temperatures,” *2018 Joint Thermophysics and Heat Transfer Conference, Atlanta*, 2018.

[25] ANSYS, Inc., *ANSYS CFX-Solver Theory Guide, Release 14.0*, November 2011.

[26] Wilcox, D., *Turbulence Modeling for CFD*, DCW Industries, Inc., 1994.

[27] ANSYS, Inc., *ANSYS CFX-Solver Modeling Guide, Release 14.0*, November 2011.

[28] Hickel, S., Adams, N. A., and Domaradzki, J. A., “An adaptive local deconvolution method for implicit LES,” *Journal of Computational Physics*, Vol. 213, No. 1, 2006, pp. 413–436.

[29] Remmler, S., and Hickel, S., “Direct and large eddy simulation of stratified turbulence,” *International Journal of Heat and Fluid Flow*, Vol. 35, 2012, pp. 13–24.

[30] Kader, B., “Temperature and concentration profiles in fully turbulent boundary layers,” *International Journal of Heat and Mass Transfer*, Vol. 24, 1981, pp. 1541–1544.